


## Reframing droplet coalescence: Identifying the distinctive dynamics of nanofilm evolution

Jhoan Toro-Mendoza <sup>1,\*</sup> Oscar Paredes-Altuve,<sup>1,2</sup> Miguel A. Velasquez,<sup>1</sup> and Dimiter N. Petsev<sup>3</sup>

<sup>1</sup>*Instituto Venezolano de Investigaciones Científicas, Centro de Estudios Interdisciplinarios de la Física, Caracas, Venezuela*

<sup>2</sup>*Universidad de Chile, Departamento de Física, Santiago de Chile, Chile*

<sup>3</sup>*University of New Mexico, Department of Chemical and Biological Engineering, Albuquerque, New Mexico, USA*



(Received 4 February 2019; revised manuscript received 20 April 2019; published 12 September 2019)

The richness of the dynamics of the thin film formed between two coalescing Brownian droplets is presented. Simulations based on a previously developed model [Phys. Rev. E **81**, 051404 (2010)] which solves two coupled Langevin equations in the lubrication limit were performed. The time evolution of the thickness and radius of the cylindrical film is evaluated for the first time in terms of phase space, entropy of permutation, mean-square displacements, and creeping compliance. This new perspective of analysis reveals the specific and distinctive features of the nanofilm formation and breaking: (1) a well-defined attractor-type phase space which slightly become less disperse as they approach instead of single deterministic trajectories observed in hydrodynamic dominated systems, (2) complexity values larger than the ones expected for Fractional Brownian Motion, (3) a super-diffusive behavior of the film thinning but a sub-diffusive behavior of the film growing, and (4) the effective shear forces in the film that strongly depends on its configuration. Remarkably, the major role of thermal fluctuations in to modulate the strong non linear effects of hydrodynamic interactions, forcing the film to explore configurations well delimited by the potential energy.

DOI: [10.1103/PhysRevFluids.4.093604](https://doi.org/10.1103/PhysRevFluids.4.093604)

### I. INTRODUCTION

Understanding droplet coalescence is both an old and ongoing challenge. Coalescence occurs whenever the intervening separating fluid film breaks against repulsive forces between droplets. The advent of nanosystems, active matter, and smart materials, which requires the adequate manipulation of droplets as well as the proper understanding of the contact and eventual film rupture, has moved the frontiers of such a problem for the strong effects of molecular interactions and thermal disturbances at the nanoscale [1–3]. Other critical scenarios for droplet coalescence are those of highly concentrated liquid-liquid dispersions such as gels and emulsions [4–6], where the effect of deformations leads to dramatic and unexpected changes in geometry [7], viscoelastic response [8,9], phase separation [10,11] and jamming [12,13]. The main quest ahead is to compare and contrast the current understanding of coalescence of macro droplets to the description of submicron droplets whose contact is mediated by fluid nanofilms in order to find the specific and distinctive features of the film formation and rupture.

---

\*Corresponding author: [jhoantoro@gmail.com](mailto:jhoantoro@gmail.com)

Previously, we reported an algorithm based on the resolution of two coupled Langevin-type equations to generate the trajectories of both film thickness and radius [14]. In that report, the analysis focused on the suitability of the algorithm for modeling films at different physicochemical conditions. Particularly, it was analyzed the contribution of each term of the equation of motion to the evolution of the configuration of the film leading to coalescence. Here, our aim is to deepen the understanding of the nanofilm thinning process and coalescence of two oil droplets in water applying for the first time within this context concepts like permutation entropy, phase space, and creeping compliance to analyze those trajectories. With these alternative tools, it is revealed the rich and complex dynamics of the film showing the differences and similarities to those observed in larger systems and new pathways in the analysis of coalescence of Brownian emulsion droplets are put forth.

Hitherto, the main focus of attention has been paid to hydrodynamic-dominated systems where the dynamics of the film follows single and well-defined trajectories and the surface evolution exhibits dimple formation [15–17]. In that case, the time required for the breaking of a film with thickness  $h$  is estimated by  $t_c = \int dh/U$ , where  $U$  is the velocity function obtained from the resolution of the Navier-Stokes equation with the proper boundary conditions. These models have been supported by experiments revealing that droplet approach and subsequent deformation follow six stages, namely: (1) at a distance  $h_i$ , the surface of the droplets slightly deform, (2) the sign of the local curvature of the droplets change forming a bell shape called dimple, (3) the depth of the dimple evolves until the internal pressure is high enough to oppose to the increase of surface area while the droplets approach each other, (4) the dimple depth decreases until a planar circular parallel film is formed in that zone and the intervening liquid drains until (5) the droplets coalesce or (6) a stable parallel circular thin film called Newton black film finally forms when mechanical equilibrium is reached and, therefore, thermal fluctuations are barely influential [17]. On the contrary, experimental studies on liquid nanofilms actively affected by thermal fluctuations which compete with potential and hydrodynamic forces have been rather sparse, mostly due to the difficulties in directly capturing the rapid variations of the film evolution, in addition to the difficulties in measuring the actual deformation during the collision of droplets undergoing Brownian motion. These kind of films are present in the contact zone between nanodroplets where the high Laplace pressure is not enough to prevent deformation. The effects on the overall system have been demonstrated [18], although a quantitative theoretical description at the nanoscale remains elusive [1]. Actually, the applicability of continuum description to both coalescence and interfacial dynamics is under scrutiny due to the molecular effects as the scale decreases [5,19], as well as the possible existence of scaling laws governing coalescence [2,20,21].

Striking and potentially applicable new phenomena are being experimentally studied such as contactless coalescence [22], jumping droplet coalescence, active underwater droplets [23], which require a full understanding of the evolution of the separating film. A recent report from Perumanath *et al.* [24] concludes from molecular simulations that the thermal disturbances play a major role in the coalescence of two nanodroplets in vacuum leading to a stochastic behavior. In our case, the presence of water between the two droplets increases the viscous friction and lessens the effect of capillary waves while the complex role of the surface interactions is kept. We will also show that thermal disturbances strongly modulate the non linear behavior dictated by hydrodynamic interactions, forcing the film to adequately follow the pathway defined by the potential energy.

## II. NUMERICAL SCHEME

In large colliding droplets, the film radius  $r$  grows at constant film separation  $h$  forced by the action of hydrodynamic resistance [17,25,26]. In contrast, for nanosized films, it is plausible that both  $r$  and  $h$  simultaneously evolve governed by two coupled equations of evolution of the cylindrical film formed between two truncated spherical oil droplets of mass  $m$  and radius  $a$  in a medium with viscosity  $\eta$  [14]. A formal strategy is to solve the time dependent Smoluchowski equation for the probability  $P$  of one central droplet to form a planar circular film with radius  $r$  and

thickness  $h$  with another droplet of the same size  $a$  [27]

$$\frac{\partial P(r, h, t)}{\partial t} = \nabla \cdot \{D(r, h) \cdot (\nabla P(r, h, t) + P(r, h, t) \nabla \beta W(r, h))\} \quad (1)$$

where  $W$  represents the total direct interactions between the particles,  $D$  the diffusion matrix representing the hydrodynamic interactions, and  $\beta^{-1}$  the Boltzmann factor ( $k_B T$ ). The resolution of Eq. (1) gives the life time of the film, i.e., the time for the droplets to coalesce and allows one to obtain the phase space of the system. An alternative treatment of the problem is to write the Langevin equation for each variable appearing in the Smoluchowski equation and solve the coupled set to obtain the trajectories. This treatment was applied by Ermak and McCammon to formulate the widely known Brownian dynamics algorithm [28]. They demonstrated that it is possible to recreate the phase space by averaging the trajectories from several evaluations of the Langevin equations. In analogy to Brownian dynamics, it was proposed in a previous report an algorithm to model the film formed between two head-on colliding droplets in the high friction lubrication limit [14]. Written in the finite differences form, the solution for the coordinates of the Langevin coupled equations reads

$$\Delta r = \left( \frac{1}{r} \frac{\partial}{\partial r} r D_{rr}^0 + \frac{\partial}{\partial h} D_{rh}^0 \right) \Delta t - \frac{1}{k_B T} \left( D_{rr}^0 \frac{\partial W^0}{\partial h} + D_{rh}^0 \frac{\partial W^0}{\partial h} \right) \Delta t + \mathfrak{R}(\Delta t), \quad (2)$$

and

$$\Delta h = \left( \frac{1}{r} \frac{\partial}{\partial r} r D_{rh}^0 + \frac{\partial}{\partial h} D_{hh}^0 \right) \Delta t - \frac{1}{k_B T} \left( D_{hh}^0 \frac{\partial W^0}{\partial h} + D_{rh}^0 \frac{\partial W^0}{\partial r} \right) \Delta t + \mathfrak{H}(\Delta t). \quad (3)$$

The displacements  $\mathfrak{R}(\Delta t)$  and  $\mathfrak{H}(\Delta t)$  are random variables that conform to a multivariate Gaussian distribution [28]. The procedure needs a random number generator which, in our case, follows two different distributions depending on whether film thickness or radius is the case (see the Appendix in Ref. [14]). For  $\mathfrak{H}$ , the distribution used to generate the random number  $l$  is given by the Gaussian distribution  $f_G(l) = \frac{1}{\sqrt{2\pi}} e^{-l^2/2}$ . Instead, for the random numbers  $m$  necessary to generate the displacement in  $\mathfrak{R}$ , a Rayleigh distribution is used  $f_R(m) = m e^{-m^2/4}$ . Note that, by definition, the numbers obtained with the Rayleigh distribution are always positive. This means that the contribution to the film due to thermal fluctuation are in the direction of growing. This is clearly unphysical because the film radius can randomly increase or decrease as a results of the thermal disturbances. To ameliorate the situation we adopt the following procedure to ensure both positive and negative contributions to the radius film fluctuations: (1) a random Rayleigh number is generated using a suitable numerical procedure, (2) using a uniform random numbers generator a number between 0 and 1 is generated, and (3) if the latter number is less than 0.5, the Rayleigh random number is selected to be positive, otherwise is selected to be negative.

Once the random numbers are calculated, we determine the covariance matrix which is given by the diffusion tensor matrix. As it was demonstrated by Ermak and McCammon [28], the coupling between hydrodynamic interactions and random displacements are given by

$$\mathfrak{L}_i(\Delta t) = \sum_{j=1}^i \sigma_{ij} X_j, \quad (4)$$

where  $\mathfrak{L}_1 = \mathfrak{R}$ ,  $\mathfrak{L}_2 = \mathfrak{H}$ ,  $X_1 = l$ ,  $X_2 = m$ , and  $\sigma_{ij}$  represent the weighting factors calculated from

$$\sigma_{ii} = \sqrt{D_{ii} - \sum_{k=1}^{i-1} \sigma_{ik}^2}, \quad (5)$$

$$\sigma_{ij} = \left( D_{ij} - \sum_{k=1}^{j-1} \sigma_{ik} \sigma_{jk} \right) \sigma_{jj}^{-1}, \quad i > j. \quad (6)$$

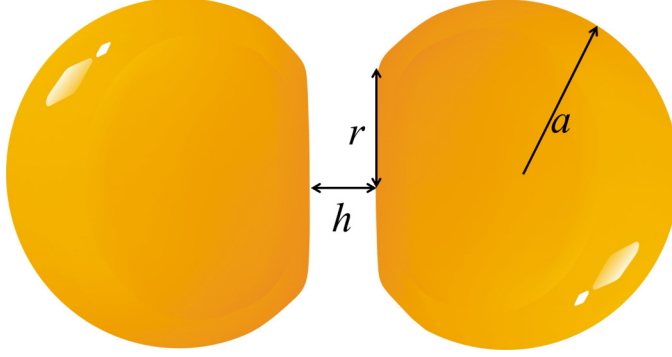


FIG. 1. Truncated spheres geometry model of two colliding emulsion droplets of size  $a$  with the cylindrical film formed between them with radius  $r$  and thickness  $h$ . In our model, both parameters vary simultaneously with time.

This procedure is known as the Choleski decomposition [29,30]. The matrix  $\sigma\sigma^t = 2\mathbf{D}\delta t$ , the diffusion tensor is given by  $\mathbf{D} = k_B T \boldsymbol{\zeta}^{-1}$ , and the elements obtained in the lubrication limit are  $\zeta_{rr} = \frac{6\pi\eta r^2}{h(1-\epsilon_s)}$ ,  $\zeta_{hh} = \frac{3\pi\eta a^2}{2h} \left(1 + \frac{r^2}{ah} + \frac{r^4}{a^2 h^2}\right)$ , and  $\zeta_{hr} = \zeta_{rh} = -\frac{3\pi\eta r^3}{h^2}$  [26].

Finally, the total interaction energy  $W$  is the sum of the van der Waals, electrostatic, and extensional components. The van der Waals interaction potential for two equally sized truncated spheres reads [25]

$$W_{\text{vdW}}(r, h) = -\frac{A_H}{12} \left( \frac{4a^2}{(2a+h)^2} + \frac{4a^2}{h(4a+h)} + 2 \ln \left[ \frac{h(4a+h)}{(2a+h)^2} \right] + \frac{128a^5 r^2}{h^2(2a+h)^3(4a+h)^2} \right), \quad (7)$$

where,  $A_H$  is the Hamaker constant. At moderately high ( $<25$  mV) and constant surface potential  $\Psi_0$ , the electrostatic potential is given by [25]

$$W_{\text{el}} = \pi\epsilon_0\epsilon\kappa\Psi_0^2 \{ [1 - \tanh(\kappa h/2)]r^2 + 2a\kappa^{-1} \ln[1 + \exp(-\kappa h)] \}, \quad (8)$$

where,  $\kappa^{-1} = (2e^2 z^2 C_{\text{el}} / \epsilon_0 \epsilon k_B T)$  is the screening Debye length for symmetric electrolytes. In absence of the Gibbs elasticity, the energy due to the surface extension is [25]

$$W_{\text{ext}} = \pi\gamma r^4 / 2a^2. \quad (9)$$

Within this scheme, the numerical experiment starts with the initial configuration of the film (the values are indicated in the captions of the figures) and the film evolves until the coalescence occurs at 1 nm of separation. The accuracy of the truncated sphere model was studied by Denkov *et al.* [31] by comparing the actual shape based on the volume conservation to the geometry shown in Fig. 1, finding errors in the total interaction potentials between 2% and 10%.

### III. RESULTS AND DISCUSSION

#### A. Configuration and velocities space

Figures 2(a) and 2(b) show the  $r-h$  configuration and velocity space ( $V_i$ ,  $i = r, h$ ) of the film during thinning, respectively. Energy contour lines in Fig. 2(a) are representative of the total interaction potential  $W = W_{\text{vdW}} + W_{\text{el}} + W_{\text{ext}}$  where the numbers in there indicate the values of the energy at that configuration. The bottom of Fig. 2(a) is the attractive zone where the droplets tend to be closer leading to film breaking ( $\sim -21k_B T$ ). For large separations, the positive energy curves are well separated allowing to the film to explore more configurations ( $\sim 7.5k_B T$ ). The asymmetry of the dispersion of velocities and the differences in the order of magnitude shown in Fig. 2(b) is

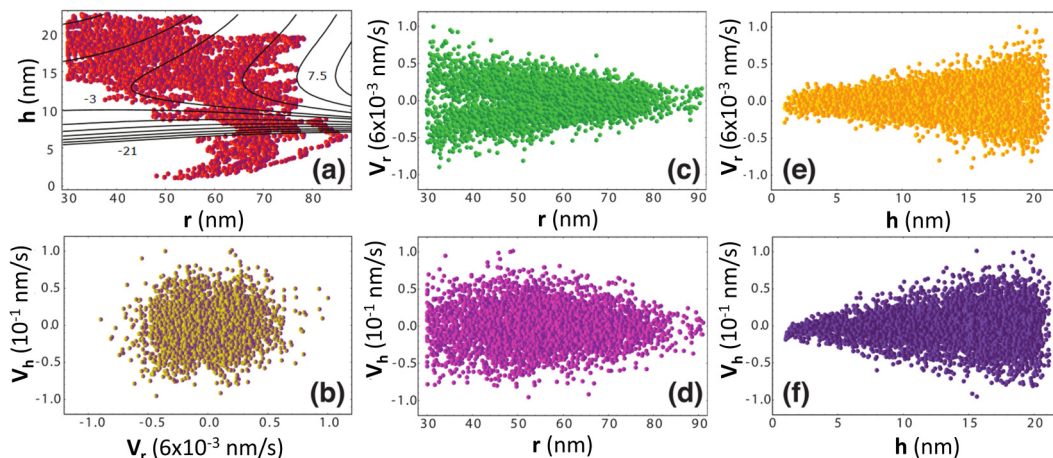


FIG. 2. Configuration space and velocities of the evolving film: (a)  $h$  vs.  $r$  with energy contour lines (separation between lines  $3 k_B T$ ; the numbers indicate the values of the energy at that configuration), (b)  $V_h$  vs.  $V_r$ , (c)  $V_r$  vs.  $r$ , (d)  $V_h$  vs.  $r$ , (e)  $V_r$  vs.  $h$ , and (f)  $V_h$  vs.  $h$ . In all these cases, the initials conditions used are  $h_0 = 20$  nm and  $r_0 = 30$  nm for 10 numerical coalescence realizations. The time step  $\Delta t \gg mD_i^0/k_B T$  was selected in accordance with the Brownian dynamic procedure for friction dominated systems ( $10^{-8}$  s). The values of parameters used are:  $a = 1 \mu\text{m}$ , interfacial tension  $\gamma = 1 \text{ mN/m}$ , water viscosity  $\eta = 8.91 \times 10^{-4} \text{ kg m}^{-1}\text{s}^{-1}$ , fundamental electric charge  $e = 1.60210 \times 10^{-19} \text{ C}$ , vacuum permittivity  $\epsilon_0 = 8.85 \times 10^{-12} \text{ Fm}^{-1}$ , relative dielectric constant of the water at room temperature  $\epsilon = 80.4$ , electrolyte concentration  $C_{el} = 0.5 \text{ M}$ , surface electric potential  $\Psi_0 = 15 \text{ mV}$ , and emulsion parameter  $\epsilon_s = 0.001$ . The velocities were directly calculated from  $\Delta x_i/\Delta t$ . Each run corresponded to different initial random seeds, and the averaging was obtained from 1000 runs.

an indicative of the freedom of  $h$  to explore more possible values than  $r$ . It can be understood by comparing the configurations explored during the coalescence process to the energy contour lines of Fig. 2(a). Indeed, the effect of the potential energy competes with thermal fluctuations and viscous friction. Remarkably, in absence of random forces, the strong nonlinear effects of the diffusion tensor lead to the film to perform a decrease in thickness during approach and an increase as droplets separate, as it is shown in the Appendix. Therefore, the main role of the random fluctuations is to modulate the nonlinear variations observed in the thickness evolution and constrain the film to move within the boundaries limited by the potential forces.

Figures 2(c)–2(f) depict the values of both axial and radial film velocity in  $r$  and  $h$ . As it is observed, as  $r$  decreases  $V_r$  accesses a wider number of values until it reaches more defined and delimited values dictated by the potential energy prior to coalescence. In this sense, this final configuration acts on the film as an attractor.  $V_h$  slightly depends on  $r$  for low and intermediate values, and the stronger effect is observed at the larger  $r$  values due to the high friction offered by this configuration. Both the radial and axial velocities are able to range over more values as the film thins by a combined effect of the tendency of the system to reach a favorable configuration and an increase of viscous friction, respectively. In other words, unlike large films, nanofilms execute a stochastic exploration of different possible configurations delimited by the interaction potential and governed by friction and thermal disturbances. In that sense, it is useful to quantify the separated contribution of the viscous and potential forces present in the nanofilm.

## B. Viscous and potential forces

The average individual magnitude of the forces derived from the energy potential  $\langle F_p \rangle$  and the  $h$ -component of viscous friction  $\langle F_{fh} \rangle$  are compared in Fig. 3. As the film thins both forces increase

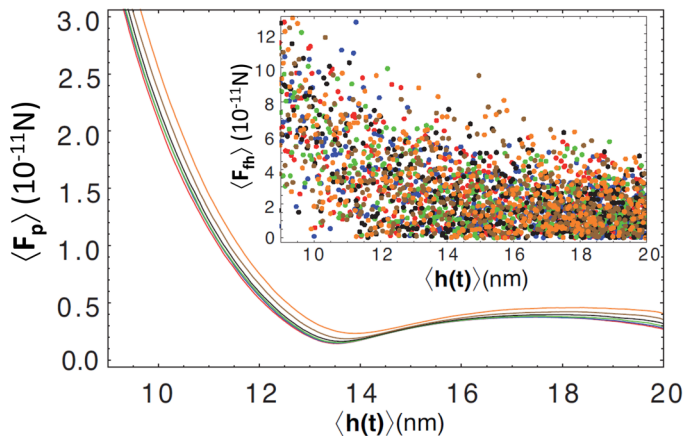


FIG. 3. Potential force during the approaching of two deformed droplets with the average distance  $\langle h \rangle$ . We use the symbols in brackets for the forces to represent their values estimated from the average values of  $r$  and  $h$ . Initial configurations of the film are  $h_0 = 20$  nm and  $r_0 = 10$  nm (red), 20 nm (blue), 40 nm (green), 50 nm (brown), and 60 nm (orange). The inset shows the average hydrodynamic friction  $F_f$  in the  $h$  direction, calculated from  $F_f = \zeta \cdot \mathbf{V}$ . Unlike the potential forces, the dispersion exhibited by  $F_{fh}$  is due to the random forces expressed through  $V$ .

in all cases for different initial film configuration. However, the potential force collapses onto one curve indicating that it affects evenly during the evolution of the film. Inversely, the average values of the  $h$  component of the friction force are dispersed and increases its magnitude as the droplets close, contrary to the results given for Fig. 2(e). The latter can also be understood by the fact that the friction is ruled by the film radius rather than the thickness, being congruent with the dispersion of the axial velocity observed in Fig. 1(c). Such a dispersion in the values of the friction is indicative that the strain response (a measure of the created surface area) of the film should vary accordingly. The force in the radial axis is two orders of magnitude lower than the axial component (not shown here) and slightly affects the dynamics. At large separations, the friction force is dominant (in average) over the potential ones. On the contrary, the magnitudes of  $\langle F_p \rangle$  and  $\langle F_{fh} \rangle$  become comparable as the droplets approach, leading to coalescence. For large films, the behavior of the thinning velocity is mainly dictated by the contour conditions to solve the Navier-Stokes equation leading to single smoothed trajectories [26]. In our case, on the contrary, the stochastic evolution of the film configurations are limited to move in a well-defined space.

### C. Mean-square radial and axial displacements

This far our analysis of the nanofilm is limited to static values. An inspection to the mean-square displacement (MSD) in both axial and radial directions shown in Figs. 4(a) and 4(b) allows to identify the impact of the potential energy and friction on the time evolution of the film. The initial stage of  $\langle \Delta r^2 \rangle (= \langle r^2 \rangle - \langle r \rangle^2)$  is typical of an anomalous diffusion process. Interestingly, after reaching a maximum,  $\langle \Delta r^2 \rangle$  decreases as a consequence of the action of the potential [see Fig. 2(f)]. An even more complex evolution is exhibited by  $\langle \Delta h^2 \rangle$  in Fig. 4(b). First, a maximum is reached at a time around  $55 \mu\text{s}$  followed by the appearance of a minimum at twice that time; after then a super-diffusive process takes place. Frequently, anomalous diffusion processes are described in terms of the viscoelastic response and a generalized Stokes-Einstein relation is used to obtain both the dissipative and the storing components [32]. In the case here observed, the storing is made by the action of the potential forces on  $r$ , as was also observed in the values for the radial velocity in Figs. 2(c) and 2(e) during the approach. The average behavior of the film thinning represented in the inset of Fig. 4(b) shows an evolution contrary to that reported for hydrodynamic-influenced systems

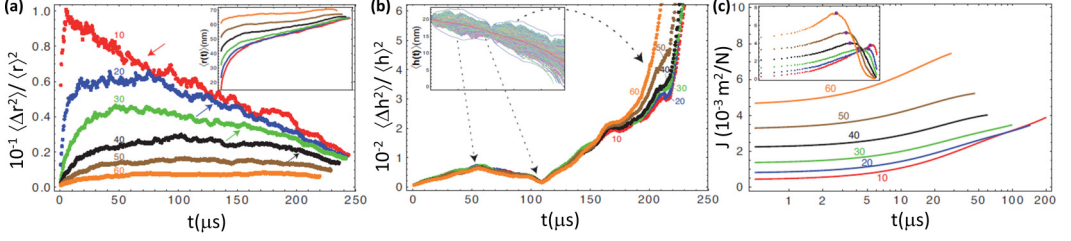


FIG. 4. Mean-square displacements in (a)  $r$  and (b)  $h$ , for initial values of  $h_0 = 20$  nm and  $r_0 = 10$  nm (red), 20 nm (blue), 30 nm (green), 40 nm (black), 50 nm (brown), and 60 nm (orange). Inset (a) average value of  $r$  for the different initial configurations and 10 realizations, and (b) average value of  $h$  (colored transparent curves; the blue envelope curves represent the standard deviation). The curves represented in (c) correspond to the creeping compliance estimated for all the mentioned cases: the inset represents the estimated values of  $J$  from  $J(t) = [A_0 - A(t)]/A_0/(\Pi - \Pi_0)$  ( $y$  axis has the same units and magnitudes that the outer curves), while outer curves in (c) correspond to the Maxwell-Kelvin phenomenological model.

where  $h$  reaches a plateau which eventually breaks [33,34]. An interesting fractal model developed by Karakashev *et al.* [35] accounts for the changes in the surface heterogeneities and the thinning velocity is predicted as

$$V_h = \frac{2h^3 \Delta P}{3\eta r^2} \left( \frac{r^2 \delta P}{16\gamma h} \right)^{(2-\beta)/(2+\beta)}, \quad (10)$$

where  $\beta$  is the fractal dimension of such heterogeneities assumed to lie between 1 and 3. In our case, that parameter should have *physical* meaningless negative values to partly reproduce our results.

#### D. Creeping compliance

It is a common practice to obtain the viscoelastic response  $\tilde{G}$  of Brownian systems from MSD curves. In our case, to obtain that information from the Laplace transformation of the curves of Figs. 3(a) and 3(b) is disadvantageous, since the application of the method developed by Mason and Weitz [32] showed inconsistencies in the obtained values. According to them,  $\tilde{G} = \frac{s}{6\pi a} [6k_B T/s^2 \langle \Delta \tilde{r}^2 \rangle - ms]$ , where  $m$  is the mass of the particle and  $s$  is the frequency of the Laplace space (we assumed that the “particle” is the film). Instead, to complement the analysis of the behavior of the film, the creeping compliance  $J$  was estimated and the results are shown in Fig. 4(c). Creeping compliance allows to probe the internal dynamics of the film as a nonequilibrium response against dilational stress [36]. This quantity is the ratio between the change in the surface area  $A$  and the applied stress  $\Pi$  as

$$J(t) = \frac{[A_0 - A(t)]/A_0}{(\Pi - \Pi_0)}. \quad (11)$$

In our case, the applied stress is given by the attractive force acting in the axial direction. In the inset of Fig. 4(c) the evolution of  $J$  directly calculated from that definition is shown. It can be noted that for the different initial values an initial region of increase of  $J$  exists until a maximum is reached and then an abrupt decrease is observed. Now, the initial region can be understood in terms of the phenomenological model of Maxwell-Kelvin [37]

$$J = \gamma_K (1 - e^{-t/(\gamma_K \eta_K)}) + \gamma_M + t/\eta_M, \quad (12)$$

where  $\eta_{M,K}$  and  $\gamma_{M,K}$  are the viscosity and interfacial tension of Maxwell and Kelvin, respectively. As known, the first term of this model accounts for the region where the delayed elastic response takes place, and the second one represents the linear response observed. It can be noticed that the evaluation of this model plotted in Fig. 4(c) shows that  $J$  is larger along the increase of  $r_0$ , a signature

TABLE I. Values of  $\gamma_{K,M}$  and  $\eta_{K,M}$  determined via Eq. (12) [see Fig. 4(c)]. The units are in MKS and  $h_0$  in nm.

| $h_0$ | $\eta_K$ | $\eta_M$       | $\gamma_K$ | $\gamma_M$ |
|-------|----------|----------------|------------|------------|
| 10    | 0.0144   | 0.1567         | 0.0022     | 0.0004     |
| 20    | 0.0139   | 0.1511         | 0.0017     | 0.0007     |
| 30    | 0.0133   | 0.1566         | 0.0015     | 0.0013     |
| 40    | 0.0119   | 3.6176         | 0.0019     | 0.0022     |
| 50    | 0.0079   | $\sim 10^{12}$ | 0.0021     | 0.0032     |
| 60    | 0.0043   | $\sim 10^{12}$ | 0.0033     | 0.0045     |

of a lower energy requirement for changing the area by the axial stress or, in other words, a lower effective shear force is needed. In Table I, the values obtained for  $\eta_{M,K}$  and  $\gamma_{M,K}$  for the different initial  $h_0$  demonstrate that the Kelvin parameters describe more adequately the evolution of the film since the values for viscosity and interfacial tension are in the order of the values used ( $\eta = 8.91 \times 10^{-4} \text{ kg m}^{-1} \text{ s}^{-1}$  and  $\gamma = \text{mN/m}$ ). However, it is also observed that the values of  $\eta_K$  are slightly larger than the viscosity of water. This is due to the additional repulsive effect of the film friction and extensional energy.

The observed increase of  $J$  is also responsible for the observed behavior of  $\langle \Delta r^2 \rangle$ : lower  $J$  allows potential forces to dominate over friction, thus reducing the possible configurations visited by  $r$ . It is worthy to mention that experiments regarding the redistribution of stresses in flowing emulsions have found that the contact zone is directly responsible for local variations of stresses affecting the overall rheological behavior [12]. Our results indirectly support these findings since small changes in the film configuration have tremendous impact on the response of the film to the action of external stresses which facilitates the appearance of heterogeneities in the interdroplet contact throughout dense moving emulsions.

### E. Complexity-entropy plane

The complex dynamics of the thinning process here observed can be quantitatively described by a complexity  $C$  and entropy  $H$  plane. Thus, the time series of both  $r$  and  $h$  are analyzed in terms of the permutation entropy introduced by Bandt and Pompe [38], which is a symbolic encoding scheme based on the ordinal relation between the amplitude of neighboring values of a given time series. In other words, permutation entropy is the Shannon entropy of the distribution of order patterns. Later, Rosso *et al.* [39] extended that methodology and introduced a representation space ( $CH$  plane) whose complexity and entropy measures are defined in terms of the probability distribution  $P$  as

$$C[P] = Q_J[P, P_e]H_S[P], \quad \text{and} \quad H_S[P] = S[P]/S_{\max}, \quad (13)$$

respectively, where  $S$  is the Shannon entropy with  $S_{\max} = S[P_e] = \ln N$  ( $0 \leq HS \leq 1$ ),  $P_e$  is the uniform distribution,  $Q_J$  is defined in terms of the extensive Jensen-Shannon divergence as

$$Q_J[P; P_e] = Q_0 S[(P + P_e)/2 - S[P]/2 - S[P_e]/2]. \quad (14)$$

To analyze the complexity and entropy of this system we use the distribution defined by Bandt and Pompe [38]. In their work, they take the time series and group the values into vectors of dimension  $n$  and then they classify them according to how their components are ordered according to its magnitude. For example, for a time series  $\{4, 5, 3, 2, 5, 1\}$ , if you want to perform the analysis for  $n = 2$ , then you must separate the vectors:  $\{4, 5\}$ ,  $\{5, 3\}$ ,  $\{3, 2\}$ ,  $\{2, 5\}$  and  $\{5, 1\}$ , which are classified according to the rule: if  $x_t < x_{t+1}$  then it is said to have order 01, whereas if they fulfill the inverse relation,  $x_{t+1} < x_t$ , then it is of order 10. With this in mind, we have a normalized discrete



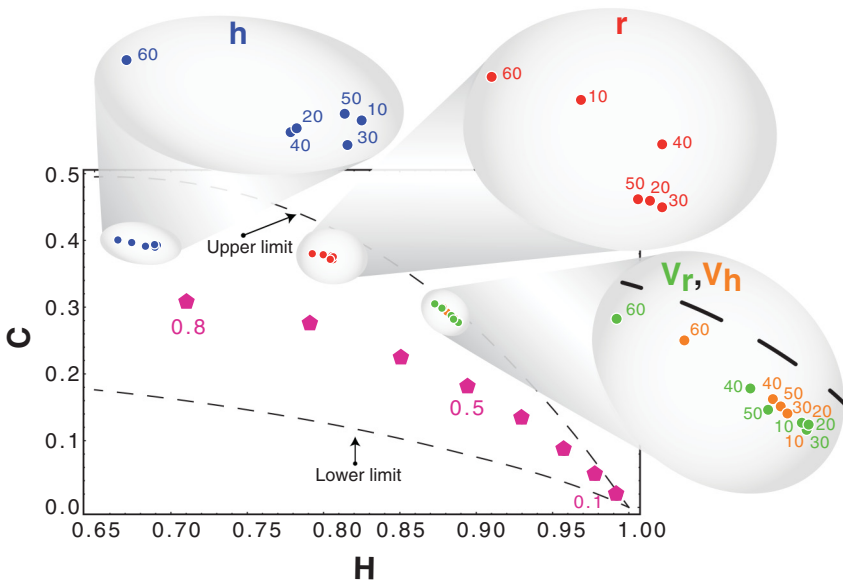


FIG. 5. Dependence of complexity  $C$  with permutation entropy  $H$  for  $h$  (blue),  $r$  (red),  $V_h$  (orange), and  $V_r$  (green). Black lines represent maximum and minimum complexities, and diamonds represent fractional Brownian motion obtained by Rosso *et al.* [39]. Entropy and complexity were calculated from the distribution permutation of dimension 6 for one realization, as proposed by Bandt and Pompe [38]. From it, the Shannon entropy and complexity were derived. This was applied to the different sets of initial parameters using the averaged values of ten runs.

distribution  $P$ , with values  $P(01) = 2/5$  and  $P(10) = 3/5$ , on which we can determine its entropy using the Shannon's formula.

In Fig. 5 we have plotted the right-hand region of the  $CH$  plane, since it is the region where it is expected to find the fingerprint of stochastic processes. As it is mentioned in Ref. [39], it is possible to define a generalized power spectrum to fractional Brownian motion (FMB) as  $\Phi \propto |f|^{-\alpha}$  with  $\alpha = \mathcal{H} + 1$  ( $1 < \alpha < 3$ ), where  $\mathcal{H}$  is the Hurst parameter. The upper and lower limits of the complexity-entropy relation are represented in black lines, and in diamonds the values obtained for FBM for different Hurst parameter values (from right to left from  $\mathcal{H} = 0.1$  to  $\mathcal{H} = 0.8$ ). The indicated value corresponds to  $\mathcal{H} = 0.5$ , that is, the traditional Brownian motion. The Hurst coefficient is a measure of the persistence of movement in the system, i.e., for values greater than 0.5 the dynamics will persist in one direction while for values less than 0.5 the dynamics will alternate between one direction or another, it is why for  $\mathcal{H} = 0.8$  is found at small values of entropy and of greater complexity than the others. Regarding the realizations of  $h$ ,  $r$ ,  $V_h$ , and  $V_r$ , we note that they are located in the upper region indicating that it has a greater complexity than the FBM processes, this is due to the presence of the nonlinear potentials and the hydrodynamic interactions. We also observe that the axial and radial velocities are grouped in a region of less complexity and higher entropy, this being that when we are in the overdamped regime. Besides, the influence of the thermal disturbances on the distribution of the permutations is more important, so there is greater flipping in the process direction than in the case of the variables  $r$  and  $h$ . Instead, the variables  $r$  and  $h$  are in different regions, with  $h$  in a region of less entropy, forced inexorably towards smaller values, indicating that there is a preferred direction of the process. This is why we find  $h$  in a region of less entropy and greater complexity than the FBM process of  $\mathcal{H} = 0.8$ . On the contrary,  $r$  is in a region of a larger entropy than  $h$  since it presents an average growth, less accelerated than the decline of  $h$ .

#### IV. CONCLUDING REMARKS

We have used the concepts of configuration and velocity space, permutation entropy and creeping compliance to analyze the evolution of the flat cylindrical film formed between two coalescing Brownian emulsion droplets. The following distinguishing properties were discovered:

(1) Both the film configuration and velocities move in a well-delimited space defined by the combined action of interdroplet interaction and friction driven by thermal disturbances.

(2) The main role of thermal disturbances is to modulate the non linear fluctuations observed in the thickness evolution and constrain the film to evolve within the boundaries delimited by the potential forces.

(3) The configurations visited by the film becomes less dispersed as the droplets approach behaving like a sink (attractor).

(4) The *complexity* exhibited by the thinning process is larger than the one expected for Fractional Brownian Motion due to the nonlinear nature of the process.

(5) The mean-square displacement in the axial direction indicates a super-diffusive process; on the contrary, a sub-diffusive process is observed in the radial direction.

(6) The sensitivity of the creeping compliance to the film configuration could be useful in the understanding of rheology, jamming, and stability of dense emulsions, since the overall behavior of the system is representative of small changes in the intervening thin film dynamics as it was shown here.

Finally, the perspective followed here opens new possibilities in the conceptual framework used to analyze the evolution and breakup of fluid nanofilms, and to experimentally explore some of our predictions, specially those in contrast to the known behavior of macroscopic thin liquid films. In this regard, we propose to perform experiments involving interferometric measurements at the fluid/fluid film to scrutinize the fast changes dynamics observed in either the optical thickness or the refractive index of the liquid film [40].

#### ACKNOWLEDGMENTS

J.T.-M. thanks I. Bonalde and F. Sicard for fruitful discussions and criticisms. Thanks are also given to Juan Carlos Granadillos for his help in the preparation of figures. This research was funded by IVIC through the project under the ID 1013.

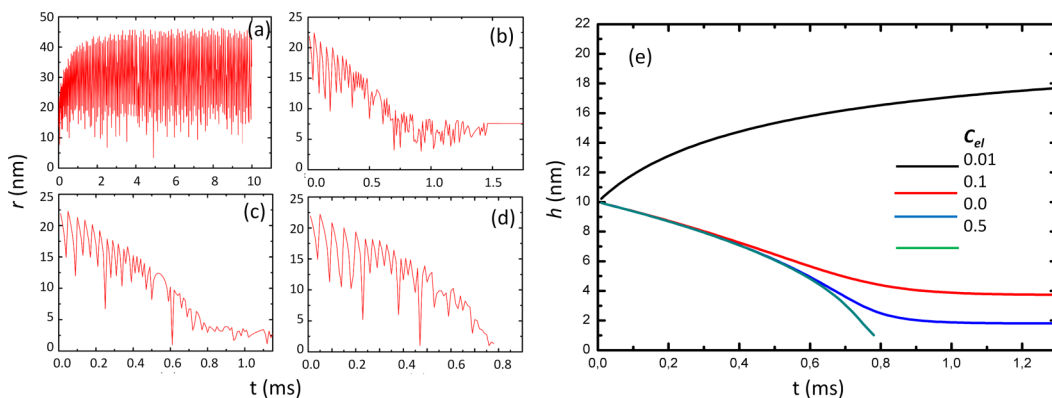


FIG. 6. Evolution of the film radius  $r$  for different electrolyte concentrations (a) 0.01 M, (b) 0.1 M, (c) 0.2 M, and (d) 0.5 M. (e) Evolution of the film thickness  $h$  leading to coalescence (color curves) and to receding (black curve).

## APPENDIX: FILM EVOLUTION IN ABSENCE OF THERMAL DISTURBANCES

In this Appendix the evolution of the film is shown in absence of random forces, i.e., when the random terms  $\mathfrak{R}$  and  $\mathfrak{S}$ , in Eqs. (2) and (3) are neglected. In Figs. 6(a)–6(c) the evolution of the film radius  $r$  is shown for different electrolyte concentration from 0.01 to 0.5 M with the rest of the parameters being the same. The role of electrolytes is to screen the electrostatic repulsion between the charged droplets. For the lower concentration, the repulsive electrostatic force prevents droplets coalescence. On the contrary, coalescence was observed for the rest of electrolyte concentrations as can be observed in Fig. 6(e). Noticeably, the nonlinear behavior which is mainly dictated by the gradients of the  $rr$  component of the diffusion tensor strongly affects the dynamic. In fact, it leads to a tendency to the film to decrease during thinning but growing during receding. Instead, a soft trajectory is exhibited by the film thickness, as Fig. 6(e) shows. Even though similar non linear terms of Eq. (2) appear in Eq. (3), the effects are less dramatic on the dynamics. Needed is to emphasize that those configurations departing from  $r \gg h$  will lie outside the applicability of the lubrication limit.

- 
- [1] F. M. Ross, Opportunities and challenges in liquid cell electron microscopy, *Science* **350**, aaa9886 (2015).
  - [2] J.-C. Pothier and L. J. Lewis, Molecular-dynamics study of the viscous to inertial crossover in nanodroplet coalescence, *Phys. Rev. B* **85**, 115447 (2012).
  - [3] D. Lohse and X. Zhang, Surface nanobubbles and nanodroplets, *Rev. Mod. Phys.* **87**, 981 (2015).
  - [4] V. V. Erramreddy, S. Tu, and S. Ghosh, Rheological reversibility and long-term stability of repulsive and attractive nanoemulsion gels, *RSC Adv.* **7**, 47818 (2017).
  - [5] R. Bardia, Z. Liang, P. Kebllinski, and M. F. Trujillo, Continuum and molecular-dynamics simulation of nanodroplet collisions, *Phys. Rev. E* **93**, 053104 (2016).
  - [6] Brian D. L., Neil Y. C. Lin, and I. Cohen, Quantitative light microscopy of dense suspensions: Colloid science at the next decimal place, *Curr. Opin. Colloid Interface Sci.* **34**, 32 (2018).
  - [7] M. Van Hecke, Jamming of soft particles: Geometry, mechanics, scaling, and isostaticity, *J. Phys. Condens. Matter* **22**, 033101 (2009).
  - [8] M. Foglino, A. N. Morozov, O. Henrich, and D. Marenduzzo, Flow of Deformable Droplets: Discontinuous Shear Thinning and Velocity Oscillations, *Phys. Rev. Lett.* **119**, 208002 (2017).
  - [9] I. Jorjadze, L.-L. Pontani, and J. Brujic, Microscopic Approach to the Nonlinear Elasticity of Compressed Emulsions, *Phys. Rev. Lett.* **110**, 048302 (2013).
  - [10] P. Poulin and J. Bibette, Wetting of Emulsions Droplets: From Macroscopic to Colloidal Scale, *Phys. Rev. Lett.* **79**, 3290 (1997).
  - [11] J. Toro-Mendoza, A. Lozsan, M. Garcia-Sucre, Aly J. Castellanos S., and G. Urbina-Villalba, Influence of droplet deformability on the coalescence rate of emulsions, *Phys. Rev. E* **81**, 011405 (2010).
  - [12] K. W. Desmond and E. R. Weeks, Measurement of Stress Redistribution in Flowing Emulsions, *Phys. Rev. Lett.* **115**, 098302 (2015).
  - [13] G. M. Conle, P. Aebischer, S. Nöjd, P. Schurtenberger, and F. Scheffold, Jamming and overpacking fuzzy microgels: Deformation, interpenetration, and compression, *Sci. Adv.* **3**, e1700969 (2017).
  - [14] J. Toro-Mendoza and D. N. Petsev, Brownian dynamics of emulsion film formation and droplet coalescence, *Phys. Rev. E* **81**, 051404 (2010).
  - [15] L. Ma, C. Zhang, and J. Luo, Investigation of the film formation mechanism of oil-in-water (o/w) emulsions, *Soft Matter* **7**, 4207 (2011).
  - [16] K. Fezzaa and Y. Wang, Ultrafast X-Ray Phase-Contrast Imaging of the Initial Coalescence Phase of Two Water Droplets, *Phys. Rev. Lett.* **100**, 104501 (2008).
  - [17] I. B. Ivanov, D. S. Dimitrov, P. Somasundaran, and R. K. Jain, Thinning of films with deformable surfaces: Diffusion-controlled surfactant transfer, *Chem. Eng. Sci.* **40**, 137 (1985).
  - [18] S. Graves, K. Meleson, J. Wilking, M. Y. Lin, and T. G. Mason, Structure of concentrated nanoemulsions, *J. Chem. Phys.* **122**, 134703 (2005).

- [19] S. Kim, D. Kim, J. Kim, S. An, and W. Jhe, Direct Evidence for Curvature-Dependent Surface Tension in Capillary Condensation: Kelvin Equation at Molecular Scale, *Phys. Rev. X* **8**, 041046 (2018).
- [20] J. D. Paulsen, J. C. Burton, and S. R. Nagel, Viscous to Inertial Crossover in Liquid Drop Coalescence, *Phys. Rev. Lett.* **106**, 114501 (2011).
- [21] M. Irshad Khodabocus, M. Sellier, and V. Nock, Scaling laws of droplet coalescence: Theory and numerical simulation, *Adv. Math. Phys.* **2018**, 4906016 (2018).
- [22] A. Watanabe, K. Hasegawa, and Y. Abe, Contactless fluid manipulation in air: Droplet coalescence and active mixing by acoustic levitation, *Sci. Rep.* **8**, 10221 (2018).
- [23] T. Banno, A. Asami, N. Ueno, H. Kitahata, Y. Koyano, K. Asakura, and T. Toyota, Deformable self-propelled micro-object comprising underwater oil droplets, *Sci. Rep.* **6**, 31292 (2016).
- [24] S. Perumanath, M. K. Borg, M. V. Chubynsky, J. E. Sprittles, and J. M. Reese, Droplet Coalescence is Initiated by Thermal Motion, *Phys. Rev. Lett.* **122**, 104501 (2019).
- [25] K. D. Danov, D. N. Petsev, N. D. Denkov, and R. Borwankar, Pair interaction energy between deformable drops and bubbles, *J. Chem. Phys.* **99**, 7179 (1993).
- [26] K. D. Danov, N. D. Denkov, D. N. Petsev, I. B. Ivanov, and R. Borwankar, Coalescence dynamics of deformable brownian emulsion droplets, *Langmuir* **9**, 1731 (1993).
- [27] D. N. Petsev, Theoretical analysis of film thickness transition dynamics and coalescence of charged miniemulsion droplets, *Langmuir* **16**, 2093 (2000).
- [28] D. L. Ermak and J. A. McCammon, Brownian dynamics with hydrodynamic interactions, *J. Chem. Phys.* **69**, 1352 (1978).
- [29] W. Press, S. Teukolsky, W. Vetterling, B. Flannery, and M. Metcalf, *Numerical Recipes in Fortran 90: The Art of Scientific Computing* (Cambridge University Press, Cambridge, 1996).
- [30] M. Allen and D. Tildesley, *Computer Simulation of Liquids* (Oxford University Press, Oxford, 2017).
- [31] N. D. Denkov, D. N. Petsev, and K. D. Danov, Flocculation of deformable emulsion droplets: I. Droplet shape and line tension effects, *J. Colloid Interface Sci.* **176**, 189 (1995).
- [32] T. G. Mason and D. A. Weitz, Optical Measurements of Frequency-Dependent Linear Viscoelastic Moduli of Complex Fluids, *Phys. Rev. Lett.* **74**, 1250 (1995).
- [33] H. Zeng, B. Zhao, Y. Tian, M. Tirrell, L. G. Leal, and J. N. Israelachvili, Transient surface patterns during adhesion and coalescence of thin liquid films, *Soft Matter* **3**, 88 (2007).
- [34] A. Saboni, C. Gourdon, and A. K. Chesters, Drainage and rupture of partially mobile films during coalescence in liquid-liquid systems under a constant interaction force, *J. Colloid Interface Sci.* **175**, 27 (1995).
- [35] S. I. Karakashev, D. S. Ivanova, E. D. Manev, R. Kirilova, and R. Tsekov, An experimental test of the fractal model for drainage of foam films, *J. Colloid Interface Sci.* **353**, 206 (2011).
- [36] H. Hilles and F. Monroy, Dilational creep compliance in Langmuir polymer films, *Soft Matter* **7**, 7790 (2011).
- [37] W. Findley and F. Davis, *Creep and Relaxation of Nonlinear Viscoelastic Materials* (Courier Corporation, North Chelmsford, MA, 2013).
- [38] C. Bandt and B. Pompe, Permutation Entropy: A Natural Complexity Measure for Time Series, *Phys. Rev. Lett.* **88**, 174102 (2002).
- [39] O. A. Rosso, H. A. Larrondo, M. T. Martin, A. Plastino, and M. A. Fuentes, Distinguishing Noise from Chaos, *Phys. Rev. Lett.* **99**, 154102 (2007).
- [40] D. F. Kienle and T. L. Kuhl, Analyzing refractive index profiles of confined fluids by interferometry. Part II: Multilayer and asymmetric systems, *Anal. Chim. Acta* **936**, 236 (2016).